

LARGE-SCALE IMAGE PROCESSING WITH THE ROTSE PIPELINE FOR FOLLOW-UP OF GRAVITATIONAL WAVE EVENTS

L. K. NUTTALL¹, D. J. WHITE², P. J. SUTTON¹, E. J. DAW², V. S. DHILLON², W. ZHENG³, C. AKERLOF⁴

¹School of Physics and Astronomy, Cardiff University, Cardiff, CF24 3AA, United Kingdom

²Department of Physics and Astronomy, University of Sheffield, Sheffield, S3 7RH, United Kingdom

³Department of Astronomy, University of California, Berkeley, CA 94720-3411, USA and

⁴Randall Laboratory of Physics, University of Michigan, 450 Church Street, Ann Arbor, MI, 48109-1040, USA

Draft version April 27, 2022

ABSTRACT

Electromagnetic (EM) observations of gravitational-wave (GW) sources would bring unique insights which are not available from either channel alone. However EM follow-up of GW events presents new challenges. GW events will have large sky error regions, on the order of 10-100 deg². Therefore there is potential for contamination by EM transients unrelated to the GW event. Furthermore, the characteristics of possible EM counterparts are uncertain, making it desirable assess the statistical significance of a candidate EM counterpart. Current image processing pipelines are not usually optimised for large-scale processing. We have automated the ROTSE image analysis, and supplemented it with a post-processing unit for candidate validation and classification. We also propose a simple *ad hoc* statistic for ranking candidates as more likely to be associated with the GW trigger. We demonstrate the performance of the automated pipeline and ranking statistic using archival ROTSE data. EM candidates from a randomly selected set of images are compared to a background estimated from the analysis of 102 additional sets of archival images. The pipeline's detection efficiency is computed empirically by re-analysis of the images after adding simulated optical transients that follow typical lightcurves for gamma-ray burst afterglows and kilonovae. The automated pipeline rejects most background events, and has $\simeq 50\%$ detection efficiency for transients up to the real limiting magnitude of the images. However $\sim 10\%$ of the image sets show a residual background tail that impedes assigning a high significance to any putative candidate. This motivates the use of information beyond simple lightcurves for background rejection.

Subject headings: gravitational waves – techniques: image processing

1. INTRODUCTION

Multi-wavelength and multi-channel observations of astrophysical systems can yield insights in to the system that are not available from a single waveband. For example, the detection of gamma-ray burst (GRB) systems in the x-ray, optical and radio bands have led to the identification of host galaxies and their redshifts, in addition to tests of theoretical models (Bloom et al. 2006; Soderberg et al. 2006; Nakar 2007). Similar benefits may be expected from multi-channel follow up of systems that emit gravitational waves (GWs). Some of the anticipated advantages include identifying host galaxies, improving parameter estimation of GW events, and determining the progenitors of phenomena such as short hard gamma-ray bursts (SGRBs); see for example Bloom et al. (2009). The first attempts to detect electromagnetic (EM) counterparts to candidate GW events were made during the 2009-2010 science run of the LIGO and Virgo detectors (Accadia et al. 2012; Abbott et al. 2009). Details on how this search was performed are documented in Abadie et al. (2011). A number of optical telescopes were triggered by the GW detectors, one such system being ROTSE-III. Given the GW detector sensitivities at the time of the search, it is unlikely that any of those triggers represent true astrophysical events. However these joint observations are a useful exercise in preparing for the era of Advanced gravitational-wave detectors (Virgo Collaboration 2009; Harry 2010; Aasi et al. 2013, c. 2015+), when EM follow-ups will be performed on GW triggers

of astrophysical origin.

The ROTSE collaboration has a well established image processing pipeline. This pipeline makes use of astronomical image subtraction by cross-convolution, removing the need for high quality reference images, with similar computational efficiency to other image processing procedures (Yuan & Akerlof 2008). Transient identification is based on human scanning of potential candidates identified by the pipeline, and separate generation of lightcurves of the most interesting candidates. The pipeline has proven to be successful in finding supernovae as well as GRB afterglows etc. (Rykoff et al. 2005; Quimby et al. 2007; Rykoff et al. 2009). However, the detection of optical transients associated to GW triggers presents new challenges, in particular the need to process large numbers of images to cover a typical GW error region, and the ability to assign a quantitative false alarm probability on any detected optical transient. It is therefore essential that we have an automated image processing pipeline, where large numbers of images can be processed.

In this paper we present modifications made to the ROTSE pipeline to allow the processing of large numbers of images with automated detection and tentative classification of transients. We evaluate the performance using archival ROTSE images, and use custom-built software to add simulated transients to images. The paper is organised as follows. In Section 2 we discuss the challenges associated with detecting an EM counterpart

to a GW event. In Section 3 we give a brief summary of the ROTSE-III telescope system as well as the images ROTSE took. In Section 4 we summarise how the ROTSE image processing pipeline identifies candidates. In Section 5 we describe the modifications made to automate the pipeline, including details of how the most significant candidates are identified as well as the simulation procedure. In Sections 6 and 7 we discuss the results of processing archival images to evaluate the optical transient background, and processing simulated transients to quantify the performance of the pipeline. We conclude with some brief comments in Section 8.

2. DETECTING AN EM COUNTERPART OF A GW EVENT

Many systems which produce detectable GWs should also be observable in EM wavebands (Abadie et al. 2011). The most promising GW sources which are also expected to have EM counterparts are mergers of binary neutron stars (NS-NS) or binaries consisting of a neutron star and stellar mass black hole (NS-BH). These systems are also the favoured progenitor model for SGRBs (Nakar 2007). Abadie et al. (2010) and Aasi et al. (2013) summarise predictions of the rate of detection of such systems by the Advanced LIGO detectors. Metzger & Berger (2012) review various possible EM counterparts. In addition to SGRBs, these include orphan optical/radio afterglows, and supernova-like optical or near-IR transients (‘kilonovae’) generated by the decay of heavy nuclei produced in the merger ejecta (Li & Paczynski 1998; Metzger et al. 2010). Another system which may produce detectable GWs are long gamma-ray bursts (LGRBs); see Abadie et al. (2012) for a summary of possible GW emission scenarios. There is a wealth of observational data detailing the afterglow of both SGRBs and LGRBs. Observations detailed in Kann et al. (2010, 2011) indicate that one day after detection, the afterglow magnitude will be in the range 18-24 for a LGRB and 24-30 for a SGRB (for a source at $z = 1$) and follow a power-law decay constant of approximately -2.6. The optical kilonova transient is expected to produce an optical emission peak at magnitude 18 at one day for a source at 50 Mpc and fade over the course of a few days (Metzger et al. 2010).

GW events which produce high-energy EM counterparts such as GRBs may be promptly identified and localised by satellites such as Swift (Gehrels et al. 2004) and Fermi (Atwood et al. 2009). However, for GW events where high-energy emission is absent, or beamed away from Earth, or where the source is outside the field of view of these satellites, the detection of an EM counterpart to a GW event will be challenging. First, sky localisation using a GW data alone will produce a large error box, typically 10 – 100 deg² (Fairhurst 2009, 2011). The field of view (FOV) of one of the ROTSE-III telescopes is ~ 3 deg², making it impractical to image the entire error region. Instead, we make use of the fact that current GW detectors had a maximum distance sensitivity of between 30-70 Mpc (for NS-NS and NS-BH binary mergers) (Abadie et al. 2010) and focus observations upon galaxies in the error region within the reach of GW detectors using the galaxy catalogue described in White et al. (2011). Despite there being hundreds of galaxies in a typical GW error box, the galaxies can be ranked according to their distance and luminosity as the most likely host from which the signal originated. Considering

a typical pointing with a ROTSE-III telescope, the probability of successfully imaging the correct host galaxy is estimated at between 30%-60%, not including galaxy catalogue incompleteness (Nuttall & Sutton 2010). For the Advanced GW detectors, which will have an order of magnitude larger distance reach (Virgo Collaboration 2009; Harry 2010), preliminary estimates indicate that at least ~ 10 pointings will be required to have reasonable probability of imaging the host galaxy (Nuttall 2013). Nissanke et al. (2013) also present strategies for identifying EM counterparts to GW mergers in the Advanced detector era.

Another complication of detecting EM counterparts to GW events is that the magnitude and decay timescale of possible EM counterparts are uncertain (Abadie et al. 2011). This uncertainty necessitates observations at both early and late times, ideally from seconds to weeks after the trigger. Combined with the large error regions associated with GW triggers, this implies the need to process many images. Given the uncertain nature of the counterpart lightcurve, the image analysis should be capable of detecting any transient that is inconsistent with typical background events (which may be real astrophysical transients unrelated to the GW trigger or image artefacts).

Finally, there has not been a confirmed detection of a GW to date, making it desirable to be able to assign a high statistical confidence in any putative EM counterpart. Analysing both ‘background’ images (images from pointings not associated with a GW trigger) and ‘injection’ images (images containing simulated transients with known lightcurves) will be vital to quantify the rate at which false transients are detected as well as the performance of the pipeline. In particular, we need to test any background rejection steps on injected transients to verify they are ‘safe’. All of these factors point to the need to automate the EM image analysis (see for example Bloom et al. 2012) to allow large-scale processing and quantitative characterisation of the pipeline.

3. THE ROTSE-III TELESCOPE SYSTEM

The Robotic Optical Transient Search Experiment (ROTSE) is dedicated to rapid follow up observations of GRBs and other fast optical transients on the time scale of seconds to days. ROTSE has undergone two phases of development thus far, ROTSE-I and III. ROTSE-I consisted of a 2 x 2 array of telephoto camera lenses co-mounted on a rapid-slewing platform, located in northern New Mexico. The array was fully automated and started taking data in 1998. Observations made by ROTSE-I of GRB 990123 revealed the first detection of an optical burst occurring during the gamma-ray emission, demonstrating the value of autonomous robotic telescope systems (Kehoe et al. 1999).

The ROTSE-III telescope system came online in 2003 and consists of four 0.45m robotic reflecting telescopes located in New South Wales, Australia (ROTSE-IIIa), Texas, USA (ROTSE-IIIb), Namibia (ROTSE-IIIc) and Turkey (ROTSE-IIId). The instruments are fully automated and make use of fast optics to give a 1.85×1.85 degree FOV. Under ideal conditions, ROTSE-III is capable of attaining 17th magnitude at the center of the FOV with a 5 second exposure, and 18.5 magnitude with a 60 second exposure. If multiple images are stacked on top

of one another or ‘coadded’ ROTSE-III can reach ~ 19 th magnitude (Smith et al. 2003). The typical limiting magnitude away from the center of the FOV is 14; this is the appropriate measure of sensitivity when searching for transients over the full 1.85×1.85 degree FOV.

Between September 2 and October 20 2010, ROTSE-III took over 700 images in response to 5 candidate GW triggers as part of the latest science run of the LIGO and Virgo detectors (Abadie et al. 2011). All four ROTSE telescopes were used to gather the images, which span from the first night following the event to one month later and vary in exposure length (either 20 or 60 seconds). When a LIGO-Virgo trigger was sent to the ROTSE telescopes, typically 30 images were taken on the first night and 8 images taken on subsequent follow-up nights, per telescope, for the first ten nights following the trigger, with additional observations around nights 15 and 30. While we do not use these images in this paper, we use archival images selected with this cadence so as to characterise the automated ROTSE pipeline in conditions matching those of GW follow-up observations.

4. THE ROTSE IMAGE PROCESSING PIPELINE

4.1. Basic features

The ROTSE image processing pipeline (Yuan & Akserlof 2008) was developed by the ROTSE collaboration to search for transient objects in images taken with the ROTSE-III telescopes. The pipeline makes use of cross-convolution to perform image subtraction. Image subtraction is an essential tool needed to remove contributions from static sources and amplify any subtle changes. For example, without image subtraction it would be almost impossible to find a source buried within a host galaxy. In this section we give a brief summary of the pipeline; more details can be found in Yuan & Akserlof (2008).

The pipeline starts by processing images through SEXTRACTOR (Bertin & Arnouts 1996), giving a list of objects with precise stellar coordinates. These coordinates are used to compute corrections for image warping, so that the stellar objects within the image overlay as closely as possible with those in the reference image. It is essential to use an image or stacked set of images (see Section 4.2) of the same region from an uninteresting time as the reference image so that a new transient may be identified. At this point in the analysis pixels within both images which exceed the saturation level are excluded. To estimate the background as precisely as possible the background difference is found between the two images, instead of the individual background for each image separately. The sky difference map is generated by performing a pixel-by-pixel subtraction between the warped and the reference image and it is this which is subtracted from the original image. The main benefit of this sky difference map is that the final subtracted image will be background-free. This procedure is repeated for all images which are to be processed before the cross-convolution algorithm is invoked.

4.2. Coadding

On a typical night, two sets of four images of 60 second exposure¹ with a 30 minute cadence are taken. These images are of the same part of the sky, so that images may be stacked on top of one another or ‘coadded’. Coadding increases, by about one magnitude, the limiting magnitude to which we are sensitive, allowing fainter objects to be seen without saturating the brightest objects within the image. Each four-image set is coadded, as well as the eight images taken for the night, resulting in three co-additions. These three images are then subtracted from the same reference image, and the three difference images processed through SEXTRACTOR to reveal the residual objects.

The ROTSE pipeline can also perform a ‘non-coadded’ analysis, in which just the images taken from the first night are processed without coadding to see if there are any fast transients on the hour time scale. Since the non-coadded analysis does not stack images, the images have a shallower limiting magnitude than those images which have been coadded. In this paper we present examples using the coadded method only, i.e. characterising the ability to detect transients with a characteristic timescale of a few days.

4.3. Candidate Selection

In the coadded analysis, we have two images made from two sets of four images (called hereafter the ‘4-fold images’) and one image made from the coadditions of all the images taken over the night (the ‘8-fold image’) as described in Section 4.2. Any residual objects identified in these images by the pipeline are required to fulfil certain criteria to be considered candidate transients, as detailed in Yuan (2010). First, the object must have a signal-to-noise ratio (SNR) above 2.5 in the 4-fold images and above 5 in the 8-fold image. Next, the position of the object between the 4-fold and 8-fold images must match to within 1.5 pixels for candidates with $\text{SNR} < 15$ and to within 1 pixel for objects with $\text{SNR} > 15$. The full width half maximum (FWHM) of the object must be no bigger than twice the median FWHM of the stars in the convolved reference image, as well as be within the range of one pixel. The change in flux is also checked in a circular region of diameter 8 pixels around the object. Different cuts are applied depending on whether the potential candidate corresponds to a stellar object or lies in a known galaxy. For example, if an object matches a star or an unknown object a flux change of 60% is required, whereas if the object is within 20% of the semi-major axis length from the galaxy centre, but not consistent with a core, only a 3% flux change is required (Yuan 2010).

After the potential candidates have gone through these checks, further criteria are applied should more than twenty candidates remain. So many candidates remaining may indicate that the subtraction did not work correctly, or that the image quality is poor. First source crowding is checked, wherein potential candidates are rejected if they have more than 15 other potential candidates with 250 pixels. If there are still more than 20 potential candidates remaining, objects near the edge of the image are discarded, since the edges are liable to fringing and aberrations (Yuan 2010). Again, if more

¹ A 20 second exposure is used if the target is in the vicinity of a bright galaxy or if the moon is in a bright phase.

than 20 potential candidates remain, the area is reduced and the process repeated until the area of the image is 800 pixels in width or there are less than 20 potential candidates remaining. In these situations it is not very likely that something of astrophysical significance will be found due to the quality of the images.

Objects which have passed all the criteria outlined above form the candidate list. In fact, several candidate lists are generated: one for each night in the coadded case, and one for each consecutive pair of images in the non-coadded case. These lists need to be combined to produce a single list of unique candidates. The vast majority ($\sim 95\%$) of these potential candidates will be image subtraction artefacts, with a minority ($\sim 2\%$) due to known variable objects such as variable stars or asteroids. We identify and remove these known transients by comparing to the SIMBAD catalogue² and the Minor Planet Checker³.

4.4. Webpages

For each candidate list the pipeline also generates a webpage such as the one shown in Figure 1. At the top of the webpage three images are shown. On the left is the coadded image for one night, in the middle is the reference image, and on the right is the subtracted image. The example subtracted image shows four candidates. Below this are a list of links, one for each candidate. Selecting a link (in this case the first) displays a table of sub-images for that candidate. The top left panel of this table shows the first coadded image (from images 1-4 taken on that night), the top middle shows the second coadded image (from images 5-8), and the top right shows the reference image, all zoomed in to the vicinity of the candidate. The bottom left plot shows the first subtracted image (the first coadded image minus the reference), the bottom middle shows the second subtracted image. The bottom right panel displays information about the candidate, including the right ascension, declination, magnitude, signal-to-noise, FWHM (these last three quantities are calculated by comparing the reference image with the coadded image of the entire night), motion (this is the variation in distance between the first and second coadded images in units of pixels), percentage flux change (between the coadded image of the night and the reference image) and whether a candidate has been found at these coordinates before. As well there are links to the SIMBAD catalogue, Minor Planet Checker, SDSS⁴, 2MASS⁵ and DSS⁶ to help decide the importance of the candidate. From this information, the user manually selects candidates of interest and lightcurves for these candidates are generated. It is possible to produce two lightcurves; one which includes both the transient and background and one which subtracts the background (estimated using an annulus of inner radius ~ 6 pixels and outer radius of ~ 14 pixels) away producing the lightcurve for just the transient.

5. AUTOMATING THE PIPELINE

² <http://simbad.u-strasbg.fr/simbad/>

³ <http://scully.cfa.harvard.edu/cgi-bin/checkmp.cgi>

⁴ <http://www.sdss.org/>

⁵ <http://www.ipac.caltech.edu/2mass/>

⁶ <http://archive.stsci.edu/cgi-bin/dssform>

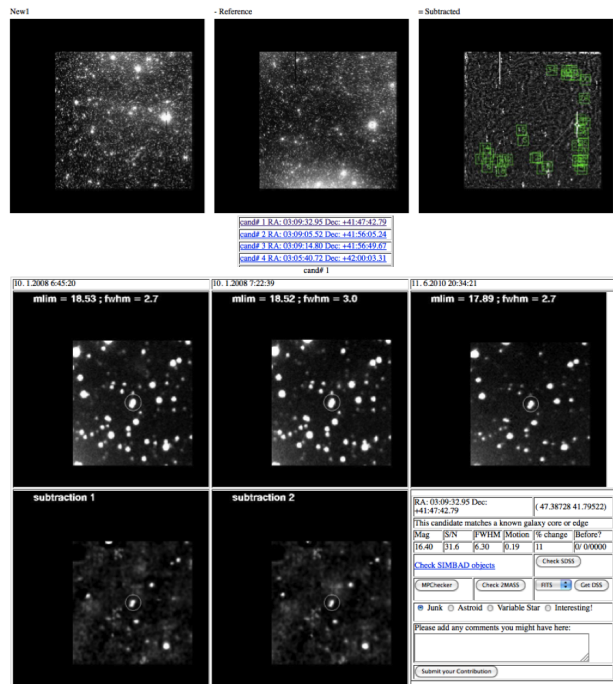


FIG. 1.— A sample ROTSE pipeline webpage, showing links to all the candidates found as well as a table displaying subimages and information for the first candidate. The full webpage displays one table for each candidate.

The ROTSE image processing pipeline has been used to make some significant discoveries of optical transients (Kehoe et al. 1999; Baykal et al. 2005; Rykoff et al. 2005; Gezari et al. 2009; Chatzopoulos et al. 2011). However the follow up of GW events requires processing larger numbers of images that is not feasible with a widget-based, user driven setup designed to handle one set of images at a time. For example, a series of commands in the IDL environment⁷ are used to produce the various lists of candidates and their corresponding webpages. Human scanning is then required to distinguish candidates of astrophysical interest from those due to poor image subtraction, those due to minor planets, etc. Further widget-based commands are then needed to produce the lightcurve of each interesting candidate. This procedure is user intensive and time consuming. However, many of these steps are algorithmic, such as checking for candidates at the same right ascension and declination across nights, and suitable for automation. We have therefore written a wrapper to the pipeline that automates the processing of large sets of images. A single command now runs the complete end-to end pipeline: looping over image sets, finding transients, identifying transients detected across multiple nights, and generating lightcurves for all transients.

Other barriers to processing large numbers of images are the need to have an IDL license for each instance of a running pipeline, and a pipeline architecture that is designed to process only a single set of events at one time. We have also altered the pipeline architecture to automatically create separate directory structures for each set of images, allow multiple instances of the pipeline

⁷ <http://www.exelisvis.com/language/en-us/products/services/idl.aspx>

to run simultaneously without conflict. Furthermore, we have removed the need for separate IDL licenses for each instance of the pipeline by compiling the pipeline in an IDL virtual machine⁸. Only one license is required, and only at the compilation stage. Combined, the change in architecture and freedom from license restrictions enables the processing of multiple sets of images simultaneously on computer clusters. We have written scripts for large scale processing using the CONDOR/DAGMAN job management system⁹ for this purpose. The automated processing is able to perform a complete analysis, identifying candidates and generating lightcurves, within a few hours (Nuttall et al. 2012). We have verified that the automated version of the pipeline produces lists of candidates which are identical to those produced by the original manual analysis.

5.1. Candidate Validation and Classification

Once the automated code has produced the lightcurve information for all the potential candidates identified by the pipeline, a series of pass/fail tests are applied to each candidate. Specifically, we test whether the candidate appears on more than one night, whether its coordinates overlap with a known variable source (by querying the SIMBAD catalogue) or with an asteroid (by querying the Minor Planet Checker), and if the lightcurve of the potential candidate varies sufficiently. This last test has two components: a check that the lightcurve decays sufficiently 48 hours after the event took place, and a chi-square test to check that the candidate’s lightcurve is not too flat. The flatness condition is

$$\chi_{\text{flat}}^2 \equiv \sum_i \left(\frac{m_i - \bar{m}}{\sigma_i} \right)^2 > 200. \quad (1)$$

Here m_i is the background-subtracted magnitude of a transient in image i with a magnitude uncertainty σ_i , and \bar{m} is the average of the m_i values. Candidates with $\chi_{\text{flat}}^2 \leq 200$ are rejected.

A least-squares linear fit in m vs. $\log_{10}[(t - t_{\text{GW}})/(1 \text{ day})]$ is used to calculate the gradient of the candidate lightcurve from 48 hours to one month after t_{GW} , the time of the event. We require a gradient ≥ 1 to pass this test. Both this threshold and the flatness threshold were selected through tests comparing lightcurve data from simulated transients and background artefacts.

The multiple-night and flatness tests are very effective at rejecting non-astrophysical background, particularly image-subtraction artefacts. We refer to these pass/fail tests collectively as the ‘hard’ cuts in the analysis. Any candidate which fails one or more of the hard cuts is discarded. The decay test is seen to reduce significantly the background of astrophysical transients unrelated to the GW trigger while not rejecting simulated astrophysical transients correlated with the GW trigger (see Section 7). The specific requirement of decay after 48 hours is motivated by models of EM counterparts for systems with strong GW emission, specifically kilonovae and SGRB/LGRB afterglows. While there are astrophysical optical transients that do not decay on this timescale, such as super-

novae (Leibundgut 2005), the expected GW emission by these sources make them less likely to produce sources of GW triggers than compact-object mergers.

The final candidate list following application of these tests typically contains fewer than 5 candidates. In order to better assess the statistical significance of any surviving candidates, we assign to each an *ad hoc* ranking statistic R defined as

$$R \equiv \sum_i \Theta(18 - m_i)(18 - m_i) \times w_i. \quad (2)$$

Here $\Theta(x)$ is the step function and w_i is a weight factor defined by

$$w_i = \begin{cases} 1 & t_i - t_{\text{GW}} < 1 \text{ day} \\ \left(1 + \log_{10} \frac{t_i - t_{\text{GW}}}{1 \text{ day}} \right)^{-a} & t_i - t_{\text{GW}} \geq 1 \text{ day} \end{cases} \quad (3)$$

Here t_{GW} is the time of the GW trigger and t_i is the time of image i . The power law index a is chosen to be 3 as shown in Figure 4 and magnitude 18 is the approximate limit at the center of the FOV for the majority of the ROTSE images we are analysing. Candidates with magnitude $m_i > 18$ are likely to be processing artefacts, so the Θ factor ensures a rank of zero for those cases. While equation (2) is *ad hoc*, it has the desirable property of favouring brighter candidates which appear in multiple images close in time to the GW trigger.

Candidates that survive the hard cuts are looked at further in two ways. Firstly we see whether the candidate’s coordinates overlap (to within three times the size of the major diameter) with a known galaxy. We use the Gravitational Wave Galaxy Catalogue (White et al. 2011), considering only galaxies within 50 Mpc, as this is approximately the maximum range of current GW detectors to NS-NS and NS-BH binaries (Abadie et al. 2011). Secondly, we perform a chi-square test comparing the candidate’s lightcurve with several theoretical models: kilonovae, SGRB afterglows, and LGRB afterglows (see Section 7). Candidates that fulfil any of these conditions are highlighted in the final candidate list, but the ranking is not altered.

5.2. Simulated Transients & Detection Efficiency

Adding simulated transients (‘injecting’) into the ROTSE images is key to quantifying both the detection efficiency and the magnitude limit of the pipeline.

To begin, the user selects a number of real stars from the image as model stars. These stars must be sufficiently bright and isolated, so that the injection code does not take into account the flux of any unwanted stars and is able to accurately determine the point spread function (PSF) of the model star. We note that simple models for the PSF (e.g. a Gaussian) are not applicable for wide FOV images such as those from ROTSE, as the PSF varies across the image. An injection is performed by selecting a random position within 100 pixels of the model star, and selecting the distance to the source. The flux of the model star (minus the background) is scaled to follow the desired lightcurve, such as the kilonova or afterglow models discussed in Section 7. The magnitude required in each image is calculated by taking into account the time between the GW trigger and the image being taken; for our tests we assume an interval of 0.5

⁸ <http://www.exelisvis.com/language/en-us/products/services/idl/idlmodules/idlvirtualmachine.aspx>

⁹ <http://research.cs.wisc.edu/condor>

days elapsed between the trigger time and the first image (White et al. 2012).

It is vital to inject a transient not only with the correct parameters, but also with the correct background. Since the processing uses image subtraction to remove the background, the variation in background around the transient in question has to be taken into account to realistically inject a simulated transient into the ROTSE images. Simply copying a model star to a new location in the image would produce a background around the injection that is significantly higher than elsewhere in the image, as the post-injection background would comprise both the pre-injection background at that location and the background around the original model star. This could lead to the image processing pipeline identifying fainter injected transients than is realistic. We therefore scale the background around the injection by a constant amount so that the background before and after the injection is comparable; see Figure 2 for an example.

6. BACKGROUND STUDY

Assigning a statistical significance to an event identified by the pipeline as associated with a GW trigger requires quantifying the false alarm probability. This is the probability of obtaining a similar event due to background, where for our purposes ‘background’ includes both image-processing artefacts and real astrophysical transients that are not associated with a GW trigger. To quantify this probability we have performed a background study using archival ROTSE data. We selected at random 102 sets of images taken in response to non-GW pointings over 2 years. To better mimic a GW trigger follow-up, each set was required to have observations spanning at least a month. This yielded a total of 103 sets of images. One of these was selected at random to be our test ‘GW trigger’, and the other 102 were used for background estimation.

The background is characterised as follows: each set of background images is processed by the automated pipeline and the highest rank R in equation (2) is found. (If a background set has no surviving candidates after the hard cuts, a rank of zero is recorded.) The distribution of highest-ranked events for our 102 background pointing sets is shown in Figure 3. We find a bi-modal distribution where approximately 80% of the pointings having a ranking statistic of less than 1 and approximately 10% have a rank greater than 11. The highest-ranked background event has $R \sim 30$. A candidate in the GW trigger image set would therefore require $R \gtrsim 11$ ($R \gtrsim 30$) to have a false alarm probability of 0.1 (0.01) or smaller.

7. INJECTION STUDY

Our injection studies add simulated transients corresponding to SGRB afterglows, LGRB afterglows, and kilonovae into the ROTSE images. We use the following simple models for these transients¹⁰

$$m_{\text{LGRB}} = 16 + \delta + \frac{8}{3} \log_{10} \frac{t - t_{\text{GW}}}{1 \text{ day}} + 5 \log_{10} \frac{D}{D_0}, \quad (4)$$

$$m_{\text{SGRB}} = 23 + \delta + \frac{8}{3} \log_{10} \frac{t - t_{\text{GW}}}{1 \text{ day}} + 5 \log_{10} \frac{D}{D_0}, \quad (5)$$

¹⁰ Equations (5)–(7) are adapted from https://trac.ligo.caltech.edu/loocup/browser/trunk/images/catalog_search/pipeline3/mfiles.

$$m_{\text{kilo}} = 27.9 + \frac{5}{2} \log_{10} \frac{10^{42} \text{ erg s}^{-1}}{L_{\text{kilo}}} + 5 \log_{10} \frac{D}{D_0}, \quad (6)$$

where L_{kilo} is the luminosity of the kilonova,

$$L_{\text{kilo}} = \begin{cases} 10^{41.97} \text{ erg s}^{-1} \left(\frac{t - t_{\text{GW}}}{1 \text{ day}} \right)^{0.43} & t - t_{\text{GW}} < 0.7 \text{ day} \\ 10^{42} \text{ erg s}^{-1} \left(\frac{1 \text{ day}}{t - t_{\text{GW}}} \right)^{1.29} & t - t_{\text{GW}} \geq 0.7 \text{ day} \end{cases}. \quad (7)$$

Equation (4) is adapted from Kann et al. (2010) and equation (5) from Kann et al. (2011). Here δ is an offset that accounts for the range in luminosities of GRB afterglows at fixed distance; it takes values from $\delta \simeq 0$ for the brightest afterglows to $\delta \simeq 8$ for the dimmest. D is the distance to the source, and $D_0 = 6634 \text{ Mpc}$ is a reference distance corresponding to $z = 1$ (assuming $H_0 = 71 \text{ km s}^{-1} \text{ Mpc}^{-1}$, $\Omega_M = 0.27$, $\Omega_\Lambda = 0.73$). t_{GW} is the time of the trigger in the observer frame (cosmological corrections to the time are negligible for all but the brightest LGRB afterglows in our analysis). Equations (6) and (7) for the kilonova model are adapted from Metzger et al. (2010).

Since this study there has been much work in modelling kilonovae and producing more realistic and comprehensive models. Metzger & Berger (2012) present a range of plausible kilonova models which span the expected range of ejecta mass and velocity and also allow for realistic uncertainties in certain parameters. These authors specifically take in to account models put forth by Roberts et al. (2011) and Goriely et al. (2011), where the former combines hydrodynamic and full nuclear network calculations to determine the heating of ejecta material and the latter makes use of relativistic hydrodynamical simulations of mergers of binary neutron stars. Piran et al. (2013) present a large set of numerical simulations which give short lived signals in the infrared to ultraviolet regime, powered by radioactive decay, while Barnes & Kasen (2013) propose a kilonova model where the ejecta opacity is much higher than previously thought, leading to longer duration signals. In addition, progenitor models explaining the first kilonova signal detected in association with short GRB GRB130603B (Tanvir et al. 2013) have been proposed (see for example Hotokezaka et al. (2013)).

We choose to inject the three models over a similar range of magnitudes, between 8 and 17 at $t = t_{\text{GW}} + 1.5 \text{ day}$. This corresponds to distances between 0.4 and 30 Mpc for the kilonova model and larger distances for the afterglow models. Assuming $\delta = 0$ in equations (4) and (5) the corresponding SGRB and LGRB afterglow distances are larger by a factor of 11 and 290, while for $\delta = 8$ the distance factors are 0.28 and 7.2. For concreteness, we assume $\delta = 0$ for all distance plots. Example lightcurves of injected transients following the kilonova and afterglow models are shown in Figure 4. The measured magnitudes and the weight factor ω_i [equation (3)] are also shown for comparison.

We choose 14 reference stars in the first image as our models for the injections. These reference stars are spread as uniformly as possible so injection performance may be tested across the image. Each reference star is used 10 times, so that 140 injections of each model are performed at each distance.

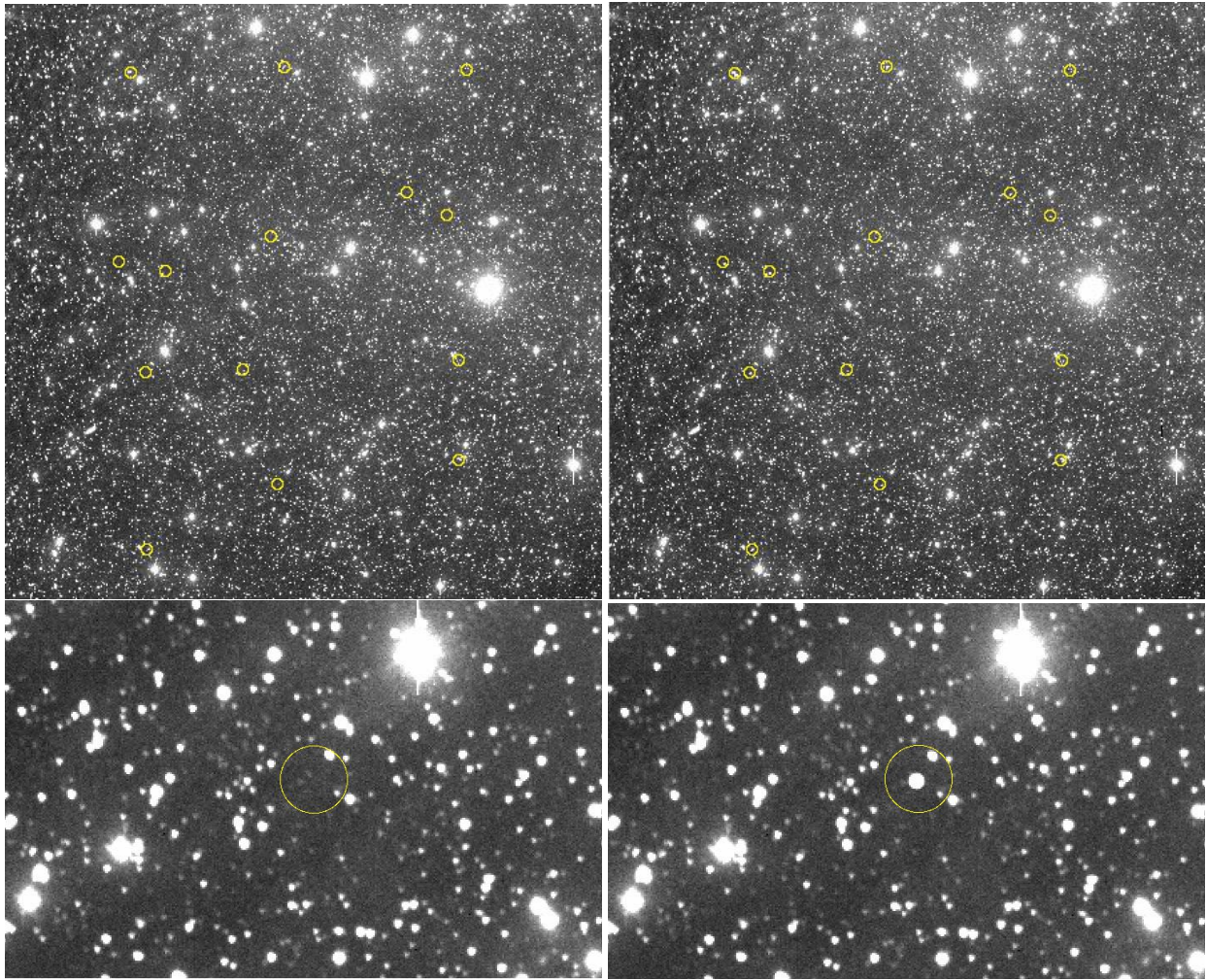


FIG. 2.— An example of injecting a number of transients into an image: (top left) original image; (top right) same image with 14 injections. The regions where the injections occurred are highlighted by yellow circles in both images for comparison. (bottom) Same images as top, focussed on the region around a single injection.

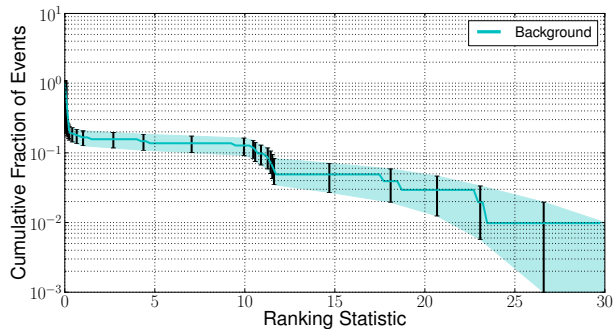


FIG. 3.— The distribution of ranking statistic R [equation (2)] for the highest-ranked transient in each of the 102 background image sets from the ROTSE archive. The error bars and shading indicate the Poisson errors for the background distribution. Image sets with no candidates surviving after the hard cuts are assigned a rank of zero. The highest-ranked background transient over the 102 sets has a rank of $R = 29.5$.

Figure 5 shows the efficiency of the pipeline in finding injections with any rank $R > 0$, in terms of distance and magnitude. The efficiency is maximum when the injection magnitude is between approximately 9 – 14 at 1.5 days after the event. This is due to the analysis requirement that the transient be seen on multiple nights;

since the lightcurves are decaying, the magnitude at 1.5 days tends to be the determining factor in whether the injection is seen on at least two nights. The efficiency drops above magnitude 14, as this is the typical limiting magnitude near the edges of the image, so injections above this in the magnitude in the outer portions of the FOV are lost. The efficiency falls to zero by magnitude 17, which is the typical limiting magnitude of the most sensitive region at the centre of the FOV.

At magnitudes below 9 the injections are so bright that their image pixels are saturated, causing the detection efficiency to drop rapidly. As described in Section 4.1, the pipeline removes saturated pixels at a very early stage as they are assumed bad and not astrophysically interesting. Attempts have been made to overcome this issue by fitting each of the injection models to the data. The best-fit model is selected and used to predict the magnitude at the time of each image. For any images for which the candidate is not reported by the pipeline and for which the predicted magnitude is low enough to cause saturation, a new rank is calculated using the predicted magnitude for that time. We find that this procedure successfully retrieves transients ~ 1 magnitude too bright for the unaltered pipeline, but it is not effective for even

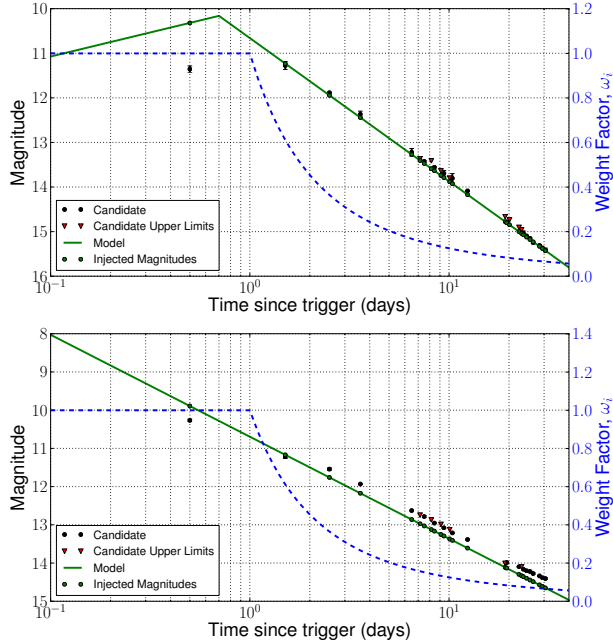


FIG. 4.— Magnitude versus time of an injected transient following the kilonova (top) and GRB afterglow (bottom) models. Shown are the transient magnitudes as reported by the automated ROTSE pipeline (black points) and upper limits for times when the transient was not found (red triangles). The magnitude of the injected transients are shown (green points) along with the model (green line). For comparison the weight factor, ω_i [equation (3)], is shown by the blue dashed line.

brighter (closer) transients. However, given the distances at which saturation occurs this is unlikely to present a problem in practice.

The maximum detection efficiency of the automated pipeline is approximately 60% to 65% for each of the models tested. Of the 35% – 40% of injections which are not found, most are lost because the background-subtracted lightcurve could not be generated. The ability of the pipeline to produce the background-subtracted lightcurve for a transient depends on both the position in the image and on the image quality, as sixteen reference stars need to be identified within a 300×300 pixel region around the transient for accurate image subtraction. Our ranking statistic R [equation (2)] is based on this lightcurve; if it is not generated then a rank $R = 0$ is assigned. If instead we were to use the non-background-subtracted light curve, the peak efficiency for each model would be closer to 90%.

The efficiencies shown in Figure 5 require only that the injection be identified with $R > 0$ and pass the hard cuts; no specific false-alarm probability threshold has been imposed. Given the large error boxes expected to be associated with GW triggers, it is desirable to be able to identify the optical counterpart with low false alarm probability. As an example, we show the efficiency of detecting injections with a false alarm probability of less than 10%. Due to the tail in the background distribution in Figure 3, this requires a relatively high rank of $R > 7 - 11.5$. The probability of detecting injections with this rank or higher is shown in Figure 6. The efficiencies are not as high as those found in Figure 5, with maximum values between $\sim 45\%$ and $\sim 60\%$ depending on the model. This would suggest that all candidates which

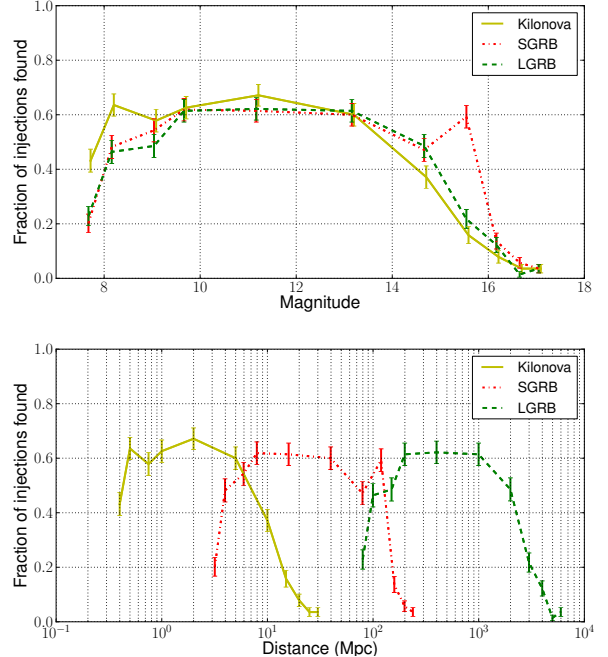


FIG. 5.— (top) Efficiency of injections found by the automated ROTSE pipeline, with $R > 0$, versus injection magnitude at 1.5 days after the trigger time. (bottom) Efficiency versus distance. The distances quoted for the GRB models assume the brightest afterglows from Kann et al. (2010, 2011); i.e. $\delta = 0$ in equations (4) and (5). The worst-case luminosities ($\delta = 8$) give distances a factor $10^{8/5} = 40$ lower. All the models suffer from poor efficiency at very close distances / low magnitudes due to saturation, while the high-magnitude cutoff corresponds to the range of limiting magnitudes across the FOV. The efficiencies reach a maximum of $\sim 60\%$ due to poor image quality in the outer parts of the FOV, as discussed in the text.

pass the hard cuts should be looked at further to see whether they are astrophysically interesting. Figure 7 shows the distribution of injections, in terms of rank, at various distances. At very close distances the rank of injections is higher than the loudest candidate found in the background. At a kilonova distance of 1 Mpc the loudest injections are comparable to the loudest background event. As the distance/magnitude is increased the ranks slowly fall to much lower numbers, making them unexceptional when compared to the loudest events in the background. This again lends weight that any candidate to make the final candidate list be further investigated for significance. It also makes clear the need for additional analysis cuts which can eliminate the tail of the background distribution seen in Figure 3.

8. CONCLUDING REMARKS

We have presented an automated pipeline for large-scale processing of images from the ROTSE-III telescope system, with features appropriate for searching for optical counterparts to gravitational-wave events. These include the ability to rapidly analyse large numbers of images, which is needed both for covering the large GW error boxes and to be able to quantitatively estimate the background of optical transients and analysis artefacts unrelated to the GW event. The pipeline also has the ability to add simulated transients to the images, which are used to determine the detection efficiency of the pipeline and to test the background-rejection steps. We

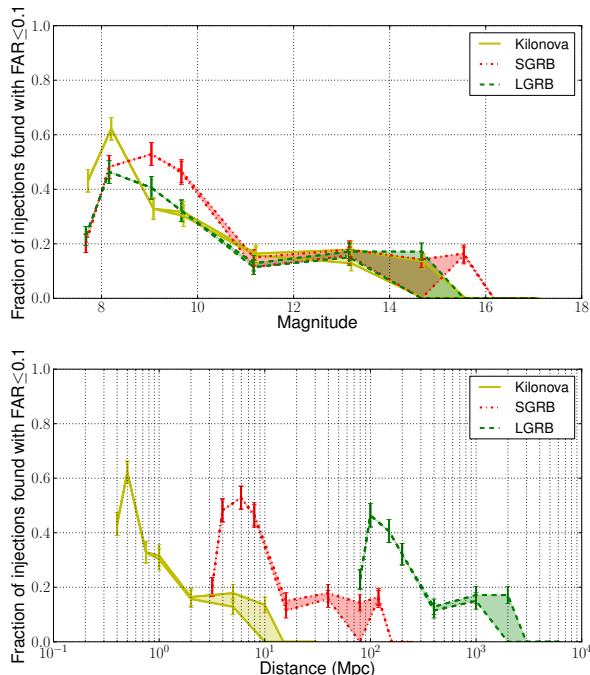


FIG. 6.— Fraction of injections found with rank $R > 7$ –11.5, for which the background false alarm probability is $< 10\%$, in terms of magnitude at 1.5 days after the trigger (top) and distance (bottom). The distances quoted for the GRB models assume the brightest afterglows from Kann et al. (2010, 2011); i.e. $\delta = 0$ in equations (4) and (5). The worst-case luminosities ($\delta = 8$) give distances a factor $10^{8/5} = 40$ lower. The shading indicates the range of efficiencies for $R > 7$ and $R > 11.5$.

have also proposed a simple ranking scheme for potential candidates. The ranking scheme favours a transient which is seen on multiple nights, has a low magnitude, and a decaying lightcurve. We have demonstrated the pipeline’s performance through a background study of more than 100 random pointings taken from the ROTSE archives, as well as an injection study of more than 4500 simulated transients added to additional archival images. We find that the automated pipeline detects more than 50% of transients with magnitudes in the range 9 – 14 at 1.5 days after the event. Injections at lower magnitudes suffer from saturation, while those at higher magnitudes exceed the limiting magnitude of the ROTSE telescopes across most of the FOV. The detection efficiency in the magnitude 9 – 14 range is limited by image quality in the outer regions of the FOV preventing construction of the background-subtracted light curve used to characterise transients.

The limited efficiency in the magnitude 9 – 14 range could be addressed by taking multiple overlapping images of the GW error box, so that any transient falls within the central $\sim 2 \text{ deg}^2$ FOV with superior limiting magnitude and image quality. (The limiting magnitude at the edge of a ROTSE image can be lower than at the centre by ~ 3 magnitudes.) This would approximately double the observation time required to cover a large error box. Alternatively, it may be possible to decrease the number of reference stars needed to generate the background-subtracted lightcurve, or to use the non-subtracted lightcurve. The main disadvantage of the latter is that the variation in the candidate’s magnitude is not easily identified due to the background.

Another concern is that the distribution of background transients (Figure 3) has a large tail from the $\sim 20\%$ of background pointings with candidates surviving the ‘hard’ cuts. Visual inspection indicates that most of these are image-subtraction artefacts. These should be identifiable by automated tests of the shape of the transient in the image, which look for ring or crescent shapes. More generally, machine-learning techniques such as those reported in Abbasi et al. (2012) could be employed to use all of the data associated with a candidate for classification. In the meantime, the presence of the background tail motivates human scanning of the handful of interesting candidates identified by the pipeline.

The advanced LIGO and Virgo detectors should commence operations in 2015 (Aasi et al. 2013). They are expected to be able to detect binary neutron star mergers to a typical distance of 200 Mpc by around the end of the decade, with expected detection rates of $0.2 \text{ yr}^{-1} - 200 \text{ yr}^{-1}$. The ROTSE limiting magnitude of 14 - 17 gives a maximum sensitive distance to kilonovae of approximately 5 Mpc, and a similar number for the dimmest SGRB afterglows. We therefore expect to require a system with limiting magnitude of approximately 20-25 to detect these counterparts at typical advanced LIGO / advanced Virgo distances (Metzger et al. 2010). The error box from GW observations will be around 10 deg^2 to 100 deg^2 . For example, simple triangulation arguments indicate that 28% of mergers will have 90% error box areas of 20 deg^2 or less (Aasi et al. 2013). This requires 5-10 tilings with the ROTSE FOV. Given the present background in the ROTSE analysis, we expect ~ 1 high-rank background event in this area, reinforcing the need for better background suppression and continued human vetting of candidates. Recently Singer et al. (2013) have demonstrated the ability to search over an error region of this size (71 deg^2) and detect the optical afterglow of a long GRB. The afterglow was identified by human scanning of 43 candidates produced by an automated analysis, and confirmed by rapid multi-wavelength followups and spectroscopic classification.

The ability to process large sets of images in a matter of hours will be essential in the advanced gravitational-wave detector era, where GW detections will be a regular occurrence. Although we know of some systems likely to produce both GW and EM transients, there are likely to be other sources we have not considered. During the next few years it is vital that we build tools to process EM data triggered from GW events in order to maximise the scientific potential of gravitational-wave observations.

9. ACKNOWLEDGMENTS

The authors thank Peter Shawhan, Jonah Kanner, Eric Chassande-Mottin and Marica Branchesi for useful discussions. We would also like to thank LIGO Laboratory and Syracuse University for use of computing clusters, with particular thanks to Duncan Brown, Peter Couvares, Ryan Fisher and Juan Barayoga. We also acknowledge NSF grants PHY-1040231, PHY-1104371, and PHY-0600953 which support Syracuse University Gravitation And Relativity computing cluster (SUGAR). ROTSE-III has been supported by NASA grant NNX-08AV63G and NSF grant PHY-0801007. LKN and DJW were supported by a STFC studentship and PJS was sup-

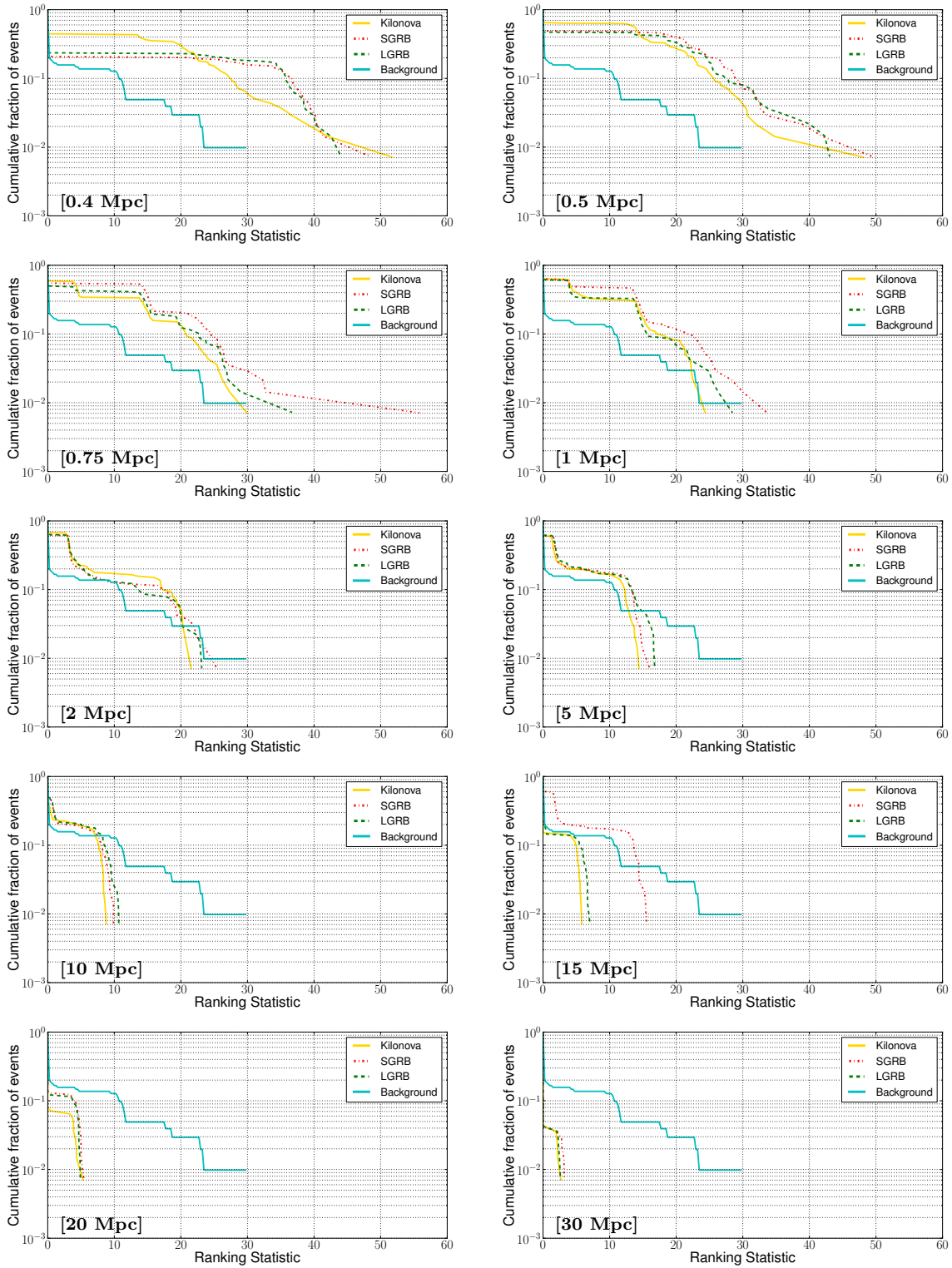


FIG. 7.— Distribution of ranking statistic values for injections and background for each injection distance. The distances quoted are those for the kilonova injections. The corresponding distances for the SGRB (LGRB) injections are larger by a factor $11 \times 10^{-\delta/5}$ ($290 \times 10^{-\delta/5}$) where δ is the magnitude offset in equations (4) and (5).

ported in part by STFC grant PP/501991. This doc-

ument has been assigned LIGO Laboratory document number LIGO-P1200131-v5.

REFERENCES

- Aasi, J., et al. 2013, arXiv:1304.0670
- Abadie, J., et al. 2010, *Class. Quant. Grav.*, 27, 173001
- . 2011, *A&A*, 539, A124
- Abadie, J., et al. 2012, *ApJ*, 760, 12
- Abbasi, R., et al. 2012, *Astron.Astrophys.*, 539, A60
- Abbott, B., et al. 2009, *Rept. Prog. Phys.*, 72, 076901
- Accadia, T., et al. 2012, *JINST*, 7, P03012
- Atwood, W. B., et al. 2009, *ApJ*, 697, 1071
- Barnes, J., & Kasen, D. 2013, *Astrophys.J.*, 775, 18
- Baykal, A., Kiziloglu, U., Kiziloglu, N., Balman, S., & Inam, S. C. 2005, *Astron.Astrophys.*
- Bertin, E., & Arnouts, S. 1996, *Astron. Astrophys. Suppl. Ser.*, 117, 393
- Bloom, J. S., Prochaska, J., Pooley, D., Blake, C., Foley, R., et al. 2006, *Astrophys.J.*, 638, 354
- Bloom, J. S., et al. 2009, arXiv:0902.1527
- Bloom, J. S., et al. 2012, *PASP*, 124, 1175
- Chatzopoulos, E., Wheeler, J. C., Vinko, J., Quimby, R., Robinson, E., et al. 2011, *Astrophys.J.*, 729, 143
- Fairhurst, S. 2009, *New J. Phys.*, 11, 123006
- . 2011, *Class.Quant.Grav.*, 28, 105021
- Gehrels, N., et al. 2004, *ApJ*, 611, 1005
- Gezari, S., Halpern, J., Grupe, D., Yuan, F., Quimby, R., et al. 2009, *Astrophys.J.*, 690, 1313
- Goriely, S., Bauswein, A., & Janka, H. 2011, *ApJ*, 738, L32
- Harry, G. M. 2010, *Class. Quant. Grav.*, 27, 084006
- Hotokezaka, K., Kyutoku, K., Tanaka, M., Kiuchi, K., Sekiguchi, Y., et al. 2013, arXiv:1310.1623
- Kann, D., Klose, S., Zhang, B., Malesani, D., Nakar, E., et al. 2010, *Astrophys.J.*, 720, 1513
- Kann, D., Klose, S., Zhang, B., Wilson, A., Butler, N., et al. 2011, *Astrophys.J.*, 734, 96
- Kehoe, R., Akerlof, C., Balsano, R., Barthelmy, S., Bloch, J., et al. 1999, arXiv:9909219
- Leibundgut, B. 2005, in *Springer Proceedings in Physics*, Vol. 99, *Cosmic Explosions*, ed. J.-M. Marcaide & K. W. Weiler (Springer Berlin Heidelberg), 173–182
- Li, L.-X., & Paczynski, B. 1998, *Astrophys.J.*, 507, L59
- Metzger, B. D., & Berger, E. 2012, *ApJ*, 746, 48
- Metzger, B. D., et al. 2010, *MNRAS*, 406, 2650
- Nakar, E. 2007, *Physics Reports*, 442, 166
- Nissanke, S., Kasliwal, M., & Georgieva, A. 2013, *Astrophys.J.*, 767, 124
- Nuttall, L., & Sutton, P. 2010, *Phys. Rev.*, D82, 102002
- Nuttall, L., et al. 2012, *J.Phys.:Conf.Ser.*, 363, 012033
- Nuttall, L.K. & Sutton, P. 2013, in preparation
- Piran, T., Nakar, E., & Rosswog, S. 2013, *MNRAS*, 430, 2121
- Quimby, R. M., Wheeler, J. C., Hofflich, P., Akerlof, C. W., Brown, P. J., et al. 2007, *Astrophys.J.*, 666, 1093
- Roberts, L., Kasen, D., Lee, W., & Ramirez-Ruiz, E. 2011, *ApJ*, 736, L21
- Rykoff, E., Aharonian, F., Akerlof, C., Ashley, M., Barthelmy, S., et al. 2009, *Astrophys.J.*, 702, 489
- Rykoff, E. S., Yost, S., Krimm, H., Aharonian, F., Akerlof, C., et al. 2005, *Astrophys.J.*, 631, L121
- Singer, L. P., Cenko, S. B., Kasliwal, M. M., Perley, D. A., Ofek, E. O., et al. 2013, arXiv:1307.5851
- Smith, D., Akerlof, C., Ashley, M., Caspersen, D., Gisler, G., et al. 2003, *AIP Conf.Proc.*, 662, 514
- Soderberg, A. M., Berger, E., Kasliwal, M., Frail, D., Price, P., et al. 2006, *Astrophys.J.*, 650, 261
- Tanvir, N., Levan, A., Fruchter, A., Hjorth, J., Wiersema, K., et al. 2013, *Nature*, 500, 547
- Virgo Collaboration. 2009, *Advanced Virgo Baseline Design*, <https://tds.ego-gw.it/itf/tds/file.php?callFile=VIR-0027A-09.pdf>
- White, D., Daw, E., & Dhillon, V. 2011, *Class.Quant.Grav.*, 28, 085016
- White, D., et al. 2012, *J.Phys.:Conf.Ser.*, 363, 012036
- Yuan, F. 2010, <http://hdl.handle.net/2027.42/75873>
- Yuan, F., & Akerlof, C. 2008, *The Astrophysical Journal*, 677, 808